Eliminating parasitic currents in the lattice Boltzmann equation method for nonideal gases

Taehun Lee[1,2,*] and Paul F. Fischer[1]
[1]*Mathematics and Computer Science Division, Argonne National Laboratory, Argonne, Illinois 60439, USA*
[2]*Department of Mechanical Engineering, The City College of the City University of New York, New York, New York 10031, USA*
(Received 28 March 2006; revised manuscript received 5 July 2006; published 25 October 2006)

A formulation of the intermolecular force in the nonideal-gas lattice Boltzmann equation method is examined. Discretization errors in the computation of the intermolecular force cause parasitic currents. These currents can be eliminated to roundoff if the potential form of the intermolecular force is used with compact isotropic discretization. Numerical tests confirm the elimination of the parasitic currents.

DOI: 10.1103/PhysRevE.74.046709 PACS number(s): 47.11.−j, 02.70.−c, 05.70.Ce

I. INTRODUCTION

The lattice Boltzmann equation (LBE) methods for nonideal gases or binary fluids have witnessed significant progress in recent years [1–16]. The success of the LBE methods can largely be attributed to their mesoscopic and kinetic nature, which enables the simulation of the macroscopic interfacial dynamics with the underlying microscopic physics. On the macroscopic level, most of these two-phase LBE methods can be considered as diffuse interface methods [17] in that the phase interface is spread on grid points and the surface tension is transformed into a volumetric force. Generally, diffuse interface methods have some advantages over sharp interface methods because computations are much easier for three-dimensional (3D) flows in which topological change of the interfaces is complicated. When applied on the uniform grid, LBE methods enjoy the unit Courant, Friedrichs, and Lewy (CFL) property that eliminates any numerical errors involved in the computation of the advection operator. The inherent isotropy of the lattice guarantees isotropic discretization of the differential operators in the LBE framework. Free from advection errors and anisotropic discretization, LBE methods can deliver much-improved solutions with the same grid resolution.

One undesirable feature of LBE methods as a diffuse interface method is the existence of parasitic currents. These currents are small-amplitude velocity fields caused by a slight imbalance between stresses in the interfacial region. Such currents increase as the surface-tension force; although they can be reduced with large viscous dissipation [18], they never disappear in most cases. They restrict the range of parameters that may be accessed by the diffuse interface method. In the case of a 2D liquid droplet immersed in a vapor phase, the flow tends to be organized into eight eddies with centers lying on the interface. In the diffuse interface method, the key to reducing the parasitic currents lies in the formulation of the surface-tension force. Jacqmin [19,20] suggested that the potential form of the surface-tension force was guaranteed to generate motionless equilibrium states without parasitic currents. Jamet *et al.*[21] later showed that the potential form ensured the correct energy transfer between the kinetic energy and the surface-tension energy, eliminating parasitic currents. Renardy and Renardy [22] also noted that the surface-tension force needs to be canceled by a pressure gradient and developed an accurate representation of the surface tension in the volume-of-fluid (VOF) context.

Several attempts have been made to reduce the magnitude of the parasitic currents and identify their origins [23–26] in the LBE framework. Nourgaliev *et al.* [23] employed a finite-difference approach in the streaming step of LBE and reported reduced currents compared with the previous LBE approaches. Lishchuk *et al.* [24] noted that the parasitic currents were unwanted artifacts originating from the mesoscopic (or microscopic) nature of LBE methods having an interface with a finite thickness, and they tried to incorporate sharp interface kinematics into their LBE method. Cristea and Sofonea [25] argued that the directional derivative operator $\mathbf{e}_\alpha \cdot \nabla$ in LBE [see Eq. (2.1)] generated parasitic currents in the interfacial region. All these LBE schemes were able to reduce the magnitude of the parasitic currents to a certain degree but never made them entirely disappear. Wagner [26] proposed that parasitic currents are caused by noncompatible discretizations of the driving forces and argued that the different discretization errors for the forces compete and drive the parasitic currents. He replaced the pressure form of the surface-tension force with the potential form of the surface-tension force and observed that the size of the maximum velocity dropped to $O(10^{-16})$. Because of the numerical instability of the LBE method, however, a tiny correction term with a small amount of numerical viscosity had to be added in his simulation.

In this paper, we will show that the potential form of the intermolecular force in the LBE context eliminates the parasitic currents and presents a stable discretization scheme. Specifically, the discrete Boltzmann equation (DBE) proposed by He *et al.* [5] is analyzed, but the analysis is equally valid for other LBE methods. Stability, order of accuracy, and isotropy of the spatial discretization are examined.

II. THEORY

The DBE with external force $\mathbf{F}$ can be written as

$$\frac{\partial f_\alpha}{\partial t} + \mathbf{e}_\alpha \cdot \nabla f_\alpha = -\frac{f_\alpha - f_\alpha^{eq}}{\lambda} + \frac{(\mathbf{e}_\alpha - \mathbf{u}) \cdot \mathbf{F}}{\rho c_s^2} f_\alpha^{eq}, \qquad (2.1)$$

where f_α is the particle distribution function, $\mathbf{e}_\alpha$ is the microscopic particle velocity, $\mathbf{u}$ is the macroscopic velocity, ρ is

*Electronic address: thlee@ccny.cuny.edu

the density, c_s is a constant, λ is the relaxation time, and $\mathbf{F}$ is the averaged external force experienced by each particle. The equilibrium distribution function f_α^{eq} is given by

$$f_\alpha^{eq} = t_\alpha \rho \left[1 + \frac{\mathbf{e}_\alpha \cdot \mathbf{u}}{c_s^2} + \frac{(\mathbf{e}_\alpha \cdot \mathbf{u})^2}{2c_s^4} - \frac{(\mathbf{u} \cdot \mathbf{u})}{2c_s^2} \right], \tag{2.2}$$

t_α being a weighting factor. In the case of a van der Waals fluid without the effect of gravity, the intermolecular attraction through the mean-field approximation and the exclusion volume of molecules yield the external force [27]

$$\mathbf{F} = \nabla(\rho c_s^2 - p_0) + \rho \kappa \nabla \nabla^2 \rho, \tag{2.3}$$

where κ is the gradient parameter and p_0 is the thermodynamic pressure that separates phases. We call this form the pressure form of the intermolecular force, or simply the pressure form.

In this model, phase separation is induced by mechanical instability in the supernodal curve of the phase diagram. Unfortunately, He and coworkers [27] reported numerical instability due to the stiffness of $\mathbf{F}$. Lee and Lin [9] later showed that the compact and isotropic finite difference yields stable discretization as long as the mechanically unstable region is resolved with enough grid points. The first term of $\mathbf{F}$ is to cancel out with the ideal-gas contribution to the pressure and may cause serious numerical instability when an inappropriate discretization scheme is used. The second term, the thermodynamic pressure gradient, is mechanically unstable in the narrow interfacial region, in which $\partial p_0 / \partial \rho$ changes its sign. The number of grid points in this region should be chosen large enough to resolve the change. The third term is associated to the interfacial stress and should balance the thermodynamic pressure gradient to maintain the equilibrium interface profile. Without this term, the interface profile would be a step function, which is numerically unsustainable unless artificial smearing of the interface is introduced, sacrificing accuracy. We note that the interfacial stress term alone does not trigger the parasitic currents. The parasitic currents are initiated by a slight imbalance between the thermodynamic pressure-gradient term and the interfacial stress term as a result of truncation error.

To avoid the truncation error, we recast Eq. (2.3) in the same form as the interfacial stress term using the thermodynamic identity. The mixing energy density for the isothermal system is

$$E_{mix}(\rho, \nabla\rho) = E_0(\rho) + \frac{\kappa}{2} |\nabla \rho|^2, \tag{2.4}$$

where the bulk energy E_0 is related to the thermodynamic pressure p_0 by the equation of state (EOS). The chemical potential is the derivative of the bulk energy with respect to the density

$$p_0 = \rho \frac{\partial E_0}{\partial \rho} - E_0, \tag{2.5}$$

$$\mu_0 = \frac{\partial E_0}{\partial \rho}. \tag{2.6}$$

Using Eq. (2.6), one can rewrite Eq. (2.3) in the potential form

$$\mathbf{F} = \nabla \rho c_s^2 - \rho \nabla (\mu_0 - \kappa \nabla^2 \rho). \tag{2.7}$$

The equilibrium profile is determined such that the energy is minimized. Now $\mu = \mu_0 - \kappa \nabla^2 \rho$ is treated as a scalar and discretized in like manner.

In the vicinity of the critical point, EOS can be simplified [28] for control of the interface thickness and surface tension at equilibrium. We assume that the bulk energy E_0 is [29]

$$E_0(\rho) \approx \beta (\rho - \rho_v^{sat})^2 (\rho - \rho_l^{sat})^2, \tag{2.8}$$

where β is a constant that is related to the compressibility of bulk phases and ρ_v^{sat} and ρ_l^{sat} are the densities of vapor and liquid phases at saturation, respectively. In a plane interface at equilibrium, the density profile across the interface is

$$\rho(z) = \frac{\rho_l^{sat} + \rho_v^{sat}}{2} + \frac{\rho_l^{sat} - \rho_v^{sat}}{2} \tanh\left(\frac{2z}{D} \right), \tag{2.9}$$

where D is the interface thickness, which is chosen based on accuracy and stability. Given D, β, and the saturation densities, one can compute the gradient parameter κ and the surface-tension force σ;

$$\kappa = \frac{\beta D^2 (\rho_l^{sat} - \rho_v^{sat})^2}{8}, \tag{2.10}$$

$$\sigma = \frac{(\rho_l^{sat} - \rho_v^{sat})^3}{6} \sqrt{2\kappa\beta}. \tag{2.11}$$

In the limiting case of zero κ, the interface thickness D goes to zero. The above simplification may cease to be valid away from the critical point, namely, at a large density difference or an equivalently low temperature. In our experience, the numerically sustainable interface thickness is $D > 3$, below which the LBE method becomes unstable or the interface shape is distorted. At large density difference, either β or σ is compromised because of the lower bound for D. Since the speed of sound is related to the bulk energy, changing β implies the modification of the speed of sound of the bulk fluid.

LBE is obtained by discretizing Eq. (2.1) along characteristics over the time step δt;

$$f_\alpha(\mathbf{x} + \mathbf{e}_\alpha \delta t, t + \delta t) - f_\alpha(\mathbf{x}, t) = -\int_t^{t+\delta t} \frac{f_\alpha - f_\alpha^{eq}}{\lambda} dt' + \int_t^{t+\delta t} \frac{(\mathbf{e}_\alpha - \mathbf{u}) \cdot (\nabla \rho c_s^2 - \rho \nabla \mu)}{\rho c_s^2} \times f_\alpha^{eq} dt'. \tag{2.12}$$

The time integration in $[t, t+\delta t]$ is coupled with the space integration in $[\mathbf{x}, \mathbf{x} + \mathbf{e}_\alpha \delta t]$. Application of the trapezoidal rule for second-order accuracy and unconditional stability leads to

$$f_\alpha(\mathbf{x}+\mathbf{e}_\alpha\delta t,t+\delta t)-f_\alpha(\mathbf{x},t)$$
$$= -\left.\frac{f_\alpha-f_\alpha^{eq}}{2\tau}\right|_{(\mathbf{x},t)} - \left.\frac{f_\alpha-f_\alpha^{eq}}{2\tau}\right|_{(\mathbf{x}+\mathbf{e}_\alpha\delta t,t+\delta t)}$$
$$+\frac{\delta t}{2}\frac{(\mathbf{e}_\alpha-\mathbf{u})\cdot(\nabla^B\rho c_s^2-\rho\nabla^B\mu)}{\rho c_s^2}f_\alpha^{eq}|_{(\mathbf{x},t)}$$
$$+\frac{\delta t}{2}\frac{(\mathbf{e}_\alpha-\mathbf{u})\cdot(\nabla^C\rho c_s^2-\rho\nabla^C\mu)}{\rho c_s^2}f_\alpha^{eq}|_{(\mathbf{x}+\mathbf{e}_\alpha\delta t,t+\delta t)}, \tag{2.13}$$

where the nondimensional relaxation time $\tau=\lambda/\delta t$ and is related to the kinematic viscosity by $\nu=\tau c_s^2\delta t$. The superscripts B and C denote the second-order biased difference and the second-order central difference, respectively, which are defined as [9]

$$\delta t\mathbf{e}_\alpha\cdot\nabla^B\rho|_{(\mathbf{x})}=\frac{-\rho(\mathbf{x}+2\mathbf{e}_\alpha\delta t)+4\rho(\mathbf{x}+\mathbf{e}_\alpha\delta t)-3\rho(\mathbf{x})}{2},$$

$$\delta t\mathbf{e}_\alpha\cdot\nabla^C\rho|_{(\mathbf{x})}=\frac{\rho(\mathbf{x}+\mathbf{e}_\alpha\delta t)-\rho(\mathbf{x}-\mathbf{e}_\alpha\delta t)}{2}. \tag{2.14}$$

Lee and Lin [9] showed that discretizations of the directional derivatives in the force terms at $(\mathbf{x})$ and $(\mathbf{x}+\mathbf{e}_\alpha\delta t)$ need to be compact around $(\mathbf{x}+\mathbf{e}_\alpha\delta t)$. Derivatives other than the directional derivatives can be obtained by taking moments of the 1D finite differences with appropriate weights yielding isotropic discretizations. The first and second derivatives are discretized as follows:

$$\nabla^B\rho|_{(\mathbf{x})}=\sum_{\alpha\neq0}\frac{t_\alpha\mathbf{e}_\alpha[-\rho(\mathbf{x}+2\mathbf{e}_\alpha\delta t)+4\rho(\mathbf{x}+\mathbf{e}_\alpha\delta t)-3\rho(\mathbf{x})]}{2c_s^2\delta t},$$

$$\nabla^C\rho|_{(\mathbf{x})}=\sum_{\alpha\neq0}\frac{t_\alpha\mathbf{e}_\alpha[\rho(\mathbf{x}+\mathbf{e}_\alpha\delta t)-\rho(\mathbf{x}-\mathbf{e}_\alpha\delta t)]}{2c_s^2\delta t},$$

$$\nabla^2\rho|_{(\mathbf{x})}=\sum_{\alpha\neq0}\frac{t_\alpha[\rho(\mathbf{x}+\mathbf{e}_\alpha\delta t)-2\rho(\mathbf{x})+\rho(\mathbf{x}-\mathbf{e}_\alpha\delta t)]}{c_s^2\delta t^2}. \tag{2.15}$$

Here, we introduce the modified particle distribution function $\bar{f}_\alpha$ and equilibrium distribution function $\bar{f}_\alpha^{eq}$ to facilitate computation;

$$\bar{f}_\alpha=f_\alpha+\frac{f_\alpha-f_\alpha^{eq}}{2\tau}-\frac{\delta t}{2}\frac{(\mathbf{e}_\alpha-\mathbf{u})\cdot(\nabla^C\rho c_s^2-\rho\nabla^C\mu)}{\rho c_s^2}f_\alpha^{eq},$$

$$\bar{f}_\alpha^{eq}=f_\alpha^{eq}-\frac{\delta t}{2}\frac{(\mathbf{e}_\alpha-\mathbf{u})\cdot(\nabla^C\rho c_s^2-\rho\nabla^C\mu)}{\rho c_s^2}f_\alpha^{eq}. \tag{2.16}$$

The density and the momentum can be computed by taking the zeroth and first moments of the modified particle distribution function

$$\rho=\sum_\alpha\bar{f}_\alpha^{eq}=\sum_\alpha\bar{f}_\alpha,$$

$$\rho\mathbf{u}=\sum_\alpha\mathbf{e}_\alpha\bar{f}_\alpha^{eq}+\frac{\delta t}{2}(\nabla^C\rho c_s^2-\rho\nabla^C\mu)$$
$$=\sum_\alpha\mathbf{e}_\alpha\bar{f}_\alpha+\frac{\delta t}{2}(\nabla^C\rho c_s^2-\rho\nabla^C\mu). \tag{2.17}$$

The space discretizations Eqs. (2.14) and (2.15) are chosen such that Eq. (2.16) exactly satisfies Eq. (2.17).

Equation (2.13) can then be recast in a simpler form,

$$\bar{f}_\alpha(\mathbf{x}+\mathbf{e}_\alpha\delta t,t+\delta t)-\bar{f}_\alpha(\mathbf{x},t)$$
$$=-\frac{1}{\tau+0.5}(\bar{f}_\alpha-\bar{f}_\alpha^{eq})|_{(\mathbf{x},t)}$$
$$+\frac{(\mathbf{e}_\alpha-\mathbf{u})\cdot(\nabla^M\rho c_s^2-\rho\nabla^M\mu)}{\rho c_s^2}f_\alpha^{eq}|_{(\mathbf{x},t)}\delta t, \tag{2.18}$$

where the superscript M denotes the second-order mixed difference defined as

$$\delta t\mathbf{e}_\alpha\cdot\nabla^M\rho=\frac{1}{2}[\delta t\mathbf{e}_\alpha\cdot\nabla^B\rho+\delta t\mathbf{e}_\alpha\cdot\nabla^C\rho], \tag{2.19}$$

$$\nabla^M\rho=\frac{1}{2}[\nabla^B\rho+\nabla^C\rho]. \tag{2.20}$$

We note that although Eq. (2.18) appears to be explicit in time, it is fully implicit for the relaxation term and the intermolecular-force terms alike and, therefore, is unconditionally stable and second-order accurate.

III. NUMERICAL TEST

The test cases confirm that the LBE method with the potential form is able to reach an equilibrium. Figure 1 shows $\rho\mathbf{u}$ fields after 100 000 time steps, when steady-state solutions are assumed. The interface thickness, droplet radius, and relaxation time are $D=4$, $R_0=25$, and $\tau=0.5$, respectively. We fixed $\beta=0.01$, $\rho_l^{sat}=1.0$, and $\rho_v^{sat}=0.1$, in which case the surface tension is $\sigma=2.187\times10^{-3}$. As initial conditions, a 2D droplet is generated at the corner of a 50×50 computational domain for a D2Q9 lattice. As a result of symmetry, a quadrant of the real domain is solved. Values of $\rho\mathbf{u}$ are magnified by 1×10^5 times in (a) and 1×10^{15} times in (b). Figure 1(a) indicates the presence of parasitic currents that are roughly aligned in the direction normal to the interface, when the pressure form of the intermolecular force is used. Away from the interface, the parasitic currents rapidly disappear.

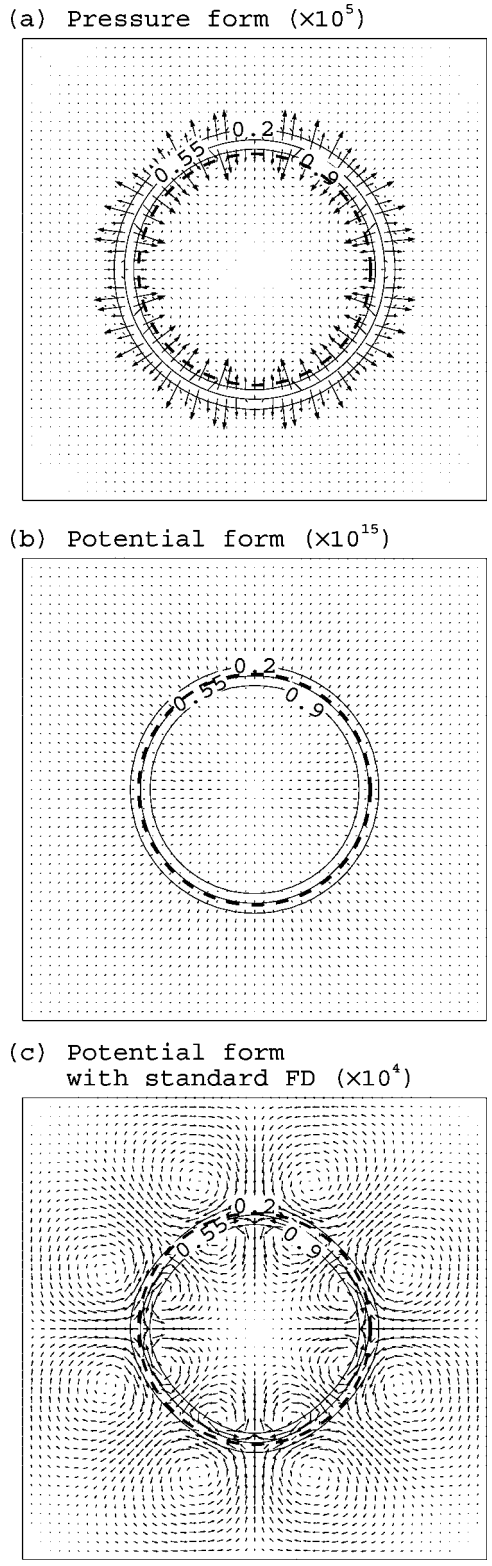

FIG. 1. $\rho\mathbf{u}$ fields after 100 000 time steps. Values of $\rho\mathbf{u}$ are magnified by 1×10^5 times in (a), 1×10^{15} times in (b), and 1×10^4 times in (c). Solid lines represent ρ=0.2, 0.55, and 0.9, and dashed lines represent the initial location of ρ=0.55.

Inexact satisfaction of $\nabla p_0=\rho\nabla\mu_0$ is responsible for the parasitic currents. Following the analysis of Jamet *et al.* [21], the discretized relation for $\nabla^C p_0|_{(\mathbf{x})}=\rho\nabla^C\mu_0|_{(\mathbf{x})}$ should be

$$\sum_{\alpha\neq0}\frac{t_\alpha\mathbf{e}_\alpha[p_0(\mathbf{x}+\mathbf{e}_\alpha\delta t)-p_0(\mathbf{x}-\mathbf{e}_\alpha\delta t)]}{2c_s^2\delta t}=\sum_{\alpha\neq0}\frac{t_\alpha\mathbf{e}_\alpha\rho[\mu_0(\mathbf{x}+\mathbf{e}_\alpha\delta t)-\mu_0(\mathbf{x}-\mathbf{e}_\alpha\delta t)]}{2c_s^2\delta t}. \quad (3.1)$$

However, the Taylor series expanding the pressure and the chemical potential reveals that the truncation error is proportional to the density gradients

$$\nabla^C p_0|_{(\mathbf{x})}-\rho\nabla^C\mu_0|_{(\mathbf{x})}=\sum_{\alpha\neq0}\frac{t_\alpha\mathbf{e}_\alpha}{6c_s^2\delta t}\left[\left(\frac{\partial\mu_0}{\partial\rho}\right)(\delta t\mathbf{e}_\alpha\cdot\nabla\rho)(\delta t\mathbf{e}_\alpha\cdot\nabla)^2\rho\right]_{(\mathbf{x})}. \quad (3.2)$$

We observe that the flow does not exhibit any organized eddies despite the presence of parasitic currents. We speculate that the absence of eddies is due to the isotropic discretization of LBE. The magnitude of the currents may be small, but the most undesirable outcome of the parasitic currents is the violation of mass conservation. Figure 1(a) shows that the droplet radius is increased after long time integration. Ideally, the net balance of mass flux across the interface region should be zero, even if the values of $\rho\mathbf{u}$ remain finite. The potential form eliminates the parasitic currents, as numerically confirmed in Fig. 1(b). Nonisotropic discretization also triggers spurious currents. Since a nonisotropic discretization such as standard central difference destabilizes the LBE method, we are unable to replace Eq. (2.15) by the standard central difference scheme. Instead, we perturb Eq. (2.15) by only 10% of the standard central difference, which is enough to break the isotropy. The modification takes the form in the x direction as

$$\nabla_x\rho|_{(\mathbf{x})}=0.9\sum_{\alpha\neq0}\frac{t_\alpha e_{x,\alpha}[\rho(\mathbf{x}+\mathbf{e}_\alpha\delta t)-\rho(\mathbf{x}-\mathbf{e}_\alpha\delta t)]}{2c_s^2\delta t}+0.1\frac{[\rho(\mathbf{x}+\Delta x)-\rho(\mathbf{x}-\Delta x)]}{2\Delta x}, \quad (3.3)$$

where Δx is the lattice spacing in the x direction. As shown in Fig. 1(c), the flow is organized into eddies, and the magnitude of the spurious currents is even higher than the pressure form.

Time evolution of the dimensionless radius for the potential form with different values of β is shown in Fig. 2. The radii of the droplet undergo rapid initial decrease and reach a steady-state value of R/R_0=0.983. The decrease in radius is because the steady-state density distribution is slightly elevated over the initial density (ρ_0) distribution due to the inclusion of radius R. Figure 3 shows the elevated steady-state density ρ and pressure p distributions over the initial distributions in the case of β=0.01. The Laplace law predicts a pressure increase for a 2D droplet, which results in a density increase

$$p_l-p_l^{sat}=\frac{\rho_l^{sat}}{\rho_l^{sat}-\rho_v^{sat}}\frac{\sigma}{R}, \quad (3.4)$$

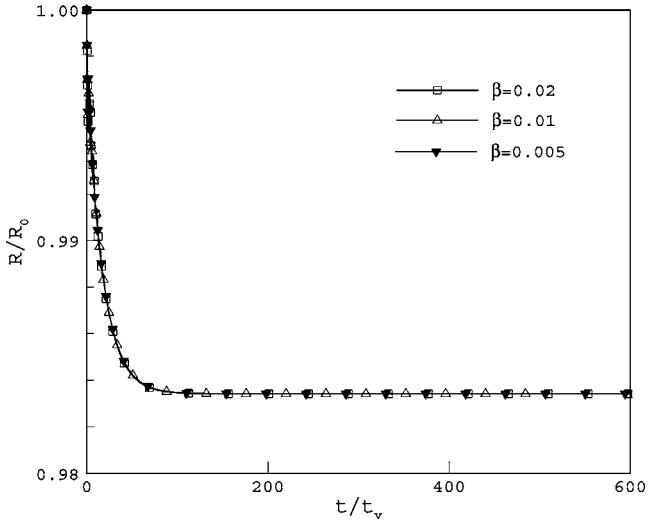

FIG. 2. Time evolution of the radius of the droplet R nondimensionalized to the initial radius R_0. τ is fixed at 0.5.

$$p_v - p_v^{sat} = \frac{\rho_v^{sat}}{\rho_l^{sat} - \rho_v^{sat}} \frac{\sigma}{R}, \tag{3.5}$$

where p_l and p_v are the pressures of liquid and vapor phases, respectively. In Fig. 3(b), p_l and p_v are in good agreement with the pressures in the bulk phases obtained from the LBE simulation. The pressure in the LBE simulation is defined by $p=p_0-\frac{\kappa}{2}\nabla\rho$. The ratio between the surface tension calculated from the pressure differences in liquid and vapor phases and the surface tension given in Eq. (2.11) is $\sigma_{LBE}/\sigma=R(p_l-p_v)_{LBE}/\sigma=0.991$.

Effects of β on the parasitic currents are examined in Fig. 4(a). The relaxation time and the interface thickness are fixed at $\tau=0.5$ and $D=4$, respectively. By fixing τ, the viscosity of the fluid is fixed. Given the interface thickness and the density ratio, higher β means higher surface-tension force as well as less compressibility, thus implying a faster convergence rate. When the time is nondimensionalized to the viscous time of the vapor phase $t_v=\rho_v^{sat}\nu_v^{sat}R_0/\sigma$, the convergence rates for different β and models collapse on a single curve. The maximum kinetic energy with the potential form decreases exponentially to roundoff. On the contrary, the maximum kinetic energy with the pressure form initially decreases at the same rate as that of the potential form but eventually stagnates. The maximum steady-state kinetic energy of the pressure form decreases with β, as the surface-tension force decreases accordingly. A similar trend can be found when β is fixed and the relaxation time τ is varied in Fig. 4(b).

We conducted comparisons of our method with previously proposed LBE models under identical computational conditions. Nourgaliev *et al.* [23] compared their model based on Swift *et al.*'s bulk energy model [3] with Shan and Chen's interparticle-interaction potential model [2]. They used the van der Waals EOS, whose free energy is $E_0=\rho RT\ln[\rho/(1-\rho b)]-a\rho^2$. In their work $a=9/49$, $b=2/21$, and $RT=0.56$ were chosen. The grid size was 100×100, the droplet radius was $R_0=20$, the relaxation time was $\tau=0.3$,

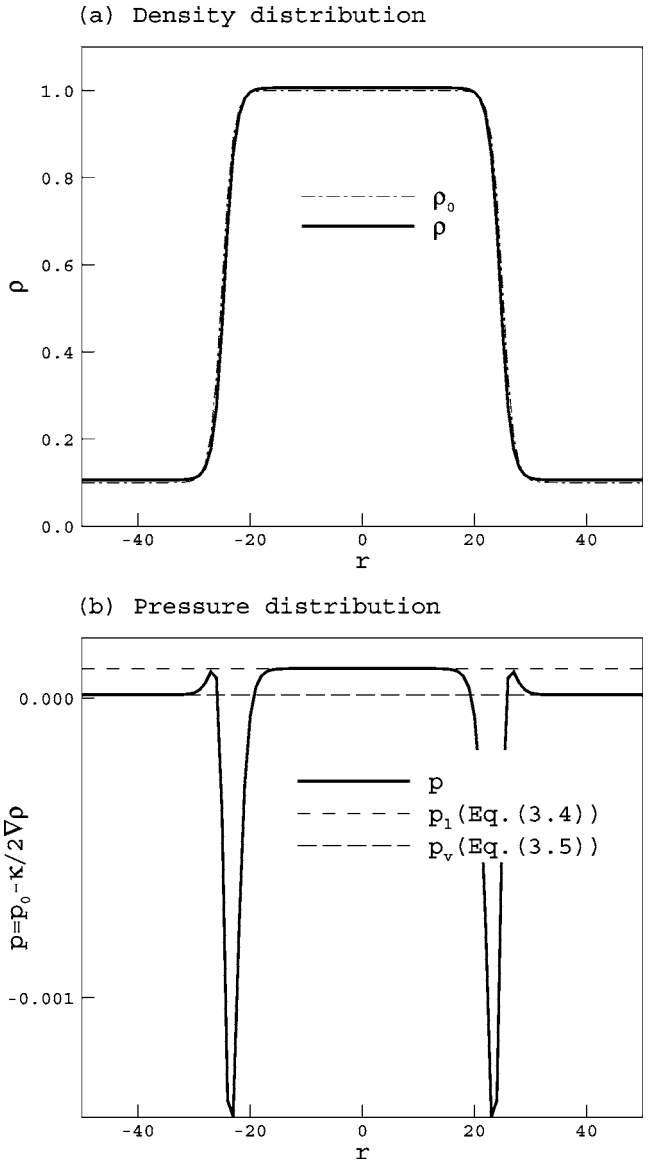

FIG. 3. (a) Density and (b) pressure distributions vs the distance from the droplet center 100 000 time steps; τ is fixed at 0.5 and β at 0.01.

and the gradient parameter was $\kappa=0.037$. We take the identical parameters and form of the free energy. Table I shows the maximum value of the parasitic currents in terms of *Mach* number. Only the present model eliminates the parasitic currents.

To test the stability of the present LBE model, we examine the inertial coalescence of droplets, driven by the surface tension. Industrial applications of this process include emulsion stability, ink-jet printing, and coating applications. At the moment of contact of droplets, the inversion of radius of curvature causes a singularity, forming a liquid bridge between the droplets. The radius of the liquid bridge R_0 then grows as $R_0(t)\propto\sqrt{t}$ by equating capillary and inertial forces. Aarts *et al.* [30] experimentally found the following prefactors for the scaling relation: water, 1.14; 5 mPa s silicon oil, 1.24; and 20 mPa s silicon oil, 1.11. Inviscid incompressible simulation by Duchemin *et al.* [31] predicted a rather large

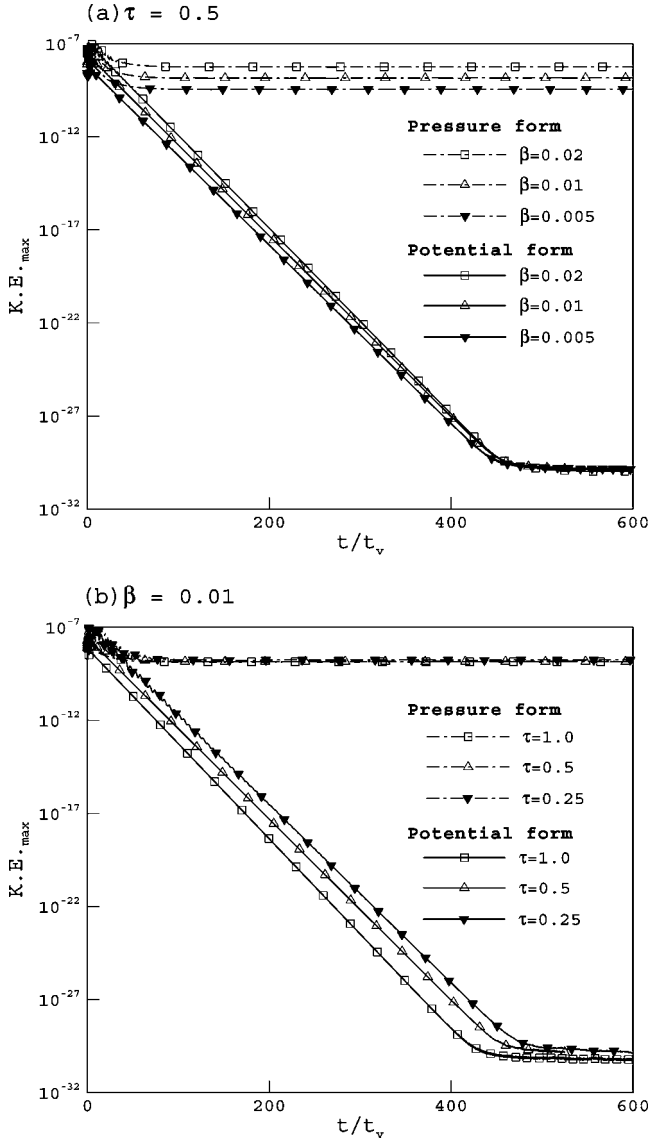

FIG. 4. Time evolution of the maximum kinetic energy for a potential form and a pressure form of the intermolecular force; τ is fixed at 0.5 in (a), while β is fixed at 0.01 in (b).

prefactor of 1.62. The initialization of simulation of coalescence is particularly challenging. Duchemin *et al.* [31] and Menchaca-Rocha *et al.* [32] smoothed the interface profile in the region of liquid bridge to avoid infinitely large capillary forces caused by the singular curvature. An effect of smoothing could be slower initial growth of the radius of the liquid bridge as a result of smaller capillary forces.

Instead of smoothing the initial profile, we choose to separate two stationary droplets by the equilibrium interface

TABLE I. Maximum value of the parasitic currents in terms of *Mach* number at steady state.

	Shan and Chen model [23]	Nourgaliev *et al.* [23]	Present
Ma_{max}	3×10^{-2}	2×10^{-4}	8×10^{-15}

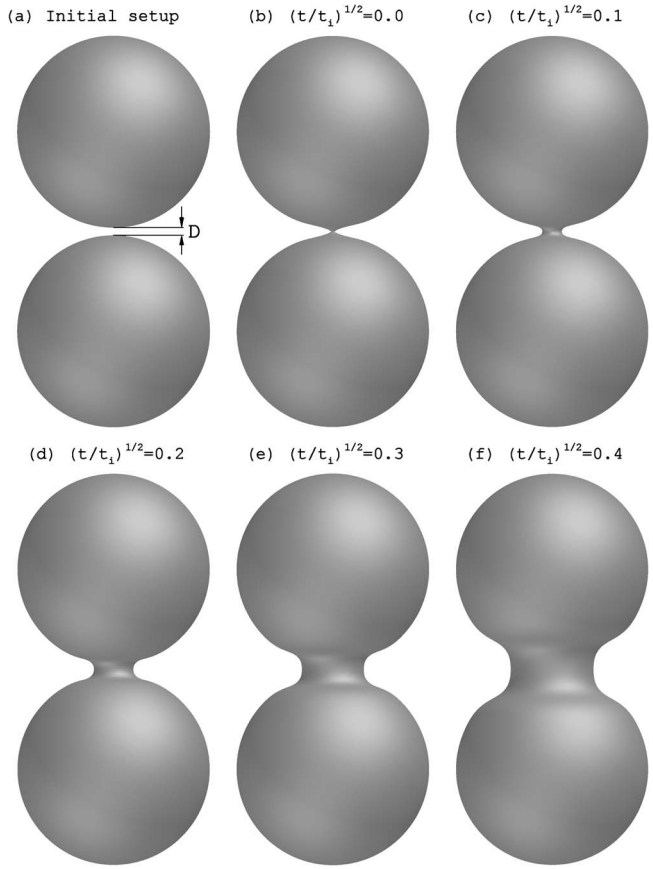

FIG. 5. Coalescence of two droplets on $200\times400\times200$ lattice at $D=4$, $R_0=50$, $\beta=0.02$, $\tau_l^{sat}=0.01$, $\tau_v^{sat}=0.2$, $\rho_l^{sat}=1.0$, and $\rho_v^{sat}=0.001$. Time is nondimensionalized to the inertial time of the liquid phase $t_i=\sqrt{\rho_l^{sat}R_0^3/\sigma}$.

thickness D as shown in Fig. 5(a). The intermolecular attraction acts at this distance and initiates the formation of the liquid bridge. Figure 5 shows coalescence of two droplets. Two 3D droplets are generated on a $200\times400\times200$ periodic computational domain for a D3Q27 lattice. The interface thickness, droplet radius, and relaxation times for liquid and vapor phases are $D=4$, $R_0=50$, and $\tau_l^{sat}=0.01$ and $\tau_v^{sat}=0.2$, respectively. We fixed $\beta=0.02$, $\rho_l^{sat}=1.0$, and $\rho_v^{sat}=0.001$. Time is nondimensionalized to the inertial time of the liquid phase $t_i=\sqrt{\rho_l^{sat}R_0^3/\sigma}$ [31] and is measured from the moment of contact [Fig. 5(b)]. The results are in good qualitative agreement with previous experimental results [30,31], except for the elongated neck region due to initial separation. The finite value of the initial separation relative to the radius of droplets can be reduced by adopting a finer mesh or an adaptive mesh refinement.

Although the approach based on free energy is derived to describe the near-critical behavior of nonideal gases at small density ratio, it is generally believed to be valid even when the density gradients become large [33]. As β decreases in the present model, however, the approximation of the bulk energy by Eq. (2.8) may become inaccurate. The effect of β on the inertial coalescence of droplets, plotted in Fig. 6, shows the time evolution of the nondimensionalized neck radii for $\beta=0.02$, 0.01, and 0.005. The differences in the

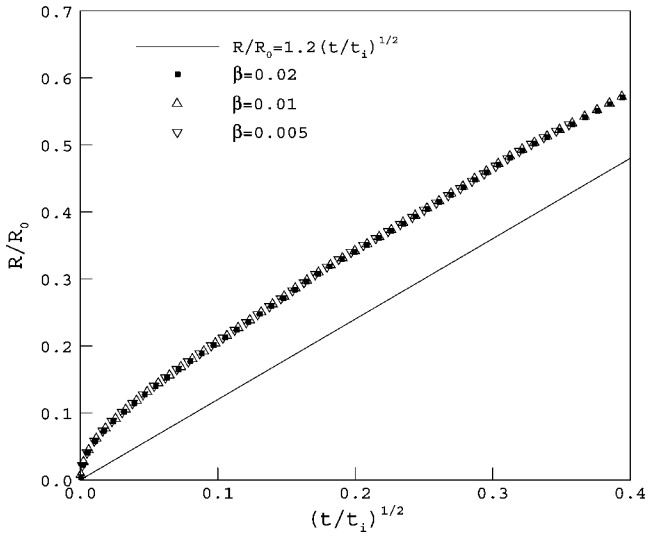

FIG. 6. Time evolution of the radius of the neck for inertia-dominated flows. The full line has a slope of 1.2 (Ref. [30]).

results are negligible in this range of β. The radii of the neck converge to the line whose slope is 1.2 [30] after rapid early growth, which is governed by the singular curvature at the moment of contact. Using an inviscid incompressible numerical method, Menchaca-Rocha *et al.* [32] reported slower initial growth of the neck radius, followed by transition region.

IV. CONCLUDING REMARKS

In summary, two different sources of error in the computation of the surface-tension force lead to the development of the parasitic currents. A slight imbalance between the pressure gradient and the stresses due to truncation error initiates the parasitic currents. As long as isotropy of the numerical scheme is retained, the parasitic currents are kept aligned in the direction normal to the interface. If isotropy is not maintained, however, the parasitic currents eventually develop into the organized flow patterns. The LBE method with isotropic discretizations can avoid the formation of these patterns. Furthermore, the use of the potential form of the intermolecular force eliminates the parasitic currents to roundoff.

ACKNOWLEDGMENTS

This work was supported in part by the Mathematical, Information, and Computational Sciences Division subprogram of the Office of Advanced Computing Research, Office of Science, U.S. Dept. of Energy, under Contract No. W-31-109-Eng-38.

[1] A. Gunstensen, D. Rothman, S. Zaleski, and G. Zanetti, Phys. Rev. A **43**, 4320 (1991).
[2] X. Shan and H. Chen, Phys. Rev. E **47**, 1815 (1993).
[3] M. Swift, W. Osborn, and J. Yeomans, Phys. Rev. Lett. **75**, 830 (1995).
[4] N. Martys and H. Chen, Phys. Rev. E **53**, 743 (1996).
[5] X. He, X. Shan, and G. Doolen, Phys. Rev. E **57**, R13 (1998).
[6] L.-S. Luo, Phys. Rev. E **62**, 4982 (2000).
[7] G. McNamara and G. Zanetti, Phys. Rev. Lett. **61**, 2332 (1988).
[8] D. Yu, R. Mei, L.-S. Luo, and W. Shyy, Prog. Aerosp. Sci. **39**, 329 (2003).
[9] T. Lee and C.-L. Lin, J. Comput. Phys. **206**, 16 (2005).
[10] L.-S. Luo and S. Girimaji, Phys. Rev. E **66**, 035301 (2002).
[11] L.-S. Luo and S. Girimaji, Phys. Rev. E **67**, 036302 (2003).
[12] A. Briant, A. Wagner, and J. Yeomans, Phys. Rev. E **69**, 031602 (2004).
[13] A. Briant and J. Yeomans, Phys. Rev. E **69**, 031603 (2004).
[14] P. Asinari, Phys. Fluids **17**, 067102 (2005).
[15] P. Asinari, Phys. Rev. E **73**, 056705 (2006).
[16] Q. Kang, D. Zhang, and S. Chen, J. Fluid Mech. **545**, 41 (2005).
[17] D. Anderson, G. McFadden, and A. Wheeler, Annu. Rev. Fluid Mech. **30**, 139 (1999).
[18] R. Scardovelli and S. Zaleski, Annu. Rev. Fluid Mech. **31**, 567 (1999).
[19] D. Jacqmin, AIAA Paper 96-0858 (1996).
[20] D. Jacqmin, J. Comput. Phys. **155**, 96 (1999).
[21] D. Jamet, D. Torres, and J. Brackbill, J. Comput. Phys. **182**, 276 (2002).
[22] Y. Renardy and M. Renardy, J. Comput. Phys. **183**, 400 (2002).
[23] R. Nourgaliev, T. Dinh, and B. Sehgal, Nucl. Eng. Des. **211**, 153 (2002).
[24] S. Lishchuk, C. Care, and I. Halliday, Phys. Rev. E **67**, 036701 (2003).
[25] A. Cristea and V. Sofonea, Int. J. Mod. Phys. C **14**, 1251 (2003).
[26] A. Wagner, Int. J. Mod. Phys. B **17**, 193 (2002).
[27] X. He, S. Chen, and R. Zhang, J. Comput. Phys. **152**, 642 (1999).
[28] J. Rowlinson and B. Widom, *Molecular Theory of Capillarity* (Dover Publications, Inc., New York, 2002).
[29] D. Jamet, O. Lebaigue, N. Coutris, and J. Delhaye, J. Comput. Phys. **169**, 624 (2001).
[30] D. Aarts, H. Lekkerkerker, H. Guo, G. Wegdam, and D. Bonn, Phys. Rev. Lett. **95**, 164503 (2005).
[31] L. Duchemin, J. Eggers, and C. Josserand, J. Fluid Mech. **487**, 167 (2003).
[32] A. Menchaca-Rocha, A. Martínez-Dávalos, R. Núñez, S. Popinet, and S. Zaleski, Phys. Rev. E **63**, 046309 (2003).
[33] J. Lowengrub and L. Truskinovsky, Proc. R. Soc. London, Ser. A **454**, 2617 (1998).